ELSEVIER

Earth and Planetary Science Letters 5863 (2001) 1–9

EPSL

www.elsevier.com/locate/epsl

Crack-induced seismic anisotropy in the oceanic crust across the East Pacific Rise (9°30′N)

Robert A. Dunn [a,*], Douglas R. Toomey [b]

[a] *Department of Geological Sciences, 1846 Brown University, Providence, RI 02912-1846, USA*
[b] *Department of Geological Sciences, 1272 University of Oregon, Eugene, OR 97412-1272, USA*

Received 12 February 2001; received in revised form 16 April 2001; accepted 17 April 2001

Abstract

The seismic anisotropy of the shallow oceanic crust across the East Pacific Rise (9°30′N) is studied with P-wave refraction data collected during a controlled-source, three-dimensional tomography experiment. The anisotropy is indicated by a $\cos(2\theta)$ pattern of travel time residuals, where θ is the receiver to shot azimuth. The travel time data are best fit by a model containing 4% anisotropy from 500 m to 1 km depth below the sea floor, 2% from 1 to 2 km, and 0% below 2 km depth. The upper 500 m of crust is not independently constrained by the data since ray paths at these depths are oriented near vertically. The fast direction of P-wave propagation is aligned along a trend oriented $6 \pm 10°$ counterclockwise from the rise axis. The results are consistent with the presence of vertically aligned cracks that form on or very near the rise axis, are oriented nearly parallel to the rise trend, penetrate to less than 2 km depth, and provide $< 10\%$ of the total pore space in the shallow crust. In comparison with similar studies across slow- and intermediate-spreading ridges, there is no apparent spreading-rate dependence of the magnitude of anisotropy.

Keywords: mid-ocean ridge; East Pacific Rise; tomography; anisotropy; oceanic crust

1. Introduction

Faults, fissures, and fractures pervade the shallow oceanic crust. The orientation of these features is sensitive to the local stress field such that they tend to align perpendicularly to the minimum compressive stress. On a scale of kilometers, the alignment is generally parallel to mid-ocean ridges. Bathymetric and side-scan sonar surveys reveal an elongate seafloor fabric that is mainly related to sets of ridge-parallel faults (e.g., [1]) and near-bottom imaging of the seafloor along mid-ocean ridges reveals fissures that tend to parallel the ridge axis (e.g., [2,3]). In addition, the subsurface detection of faults and fractures has been made by borehole measurements (e.g., [4,5]). Because the permeability of cracked rock can be several orders of magnitude larger than uncracked rock [4,6], open cracks likely provide the dominant pathways for the hydrothermal circulation that chemically alters the oceanic crust and cools ridge magmatic systems. Aligned cracks may create anisotropic permeability and perhaps

* Corresponding author. Fax: +1-401-863-2058;
E-mail: robert_allen_dunn@brown.edu
E-mail: drt@newberry.uoregon.edu

0012-821X/01/$ – see front matter © 2001 Published by Elsevier Science B.V.
PII: S0012-821X(01)00353-3

control the pattern of hydrothermal circulation [2]. However, the absence of data on the subsurface distribution of cracks inhibits our understanding of the relations between rock stresses, cracking, and the localization of hydrothermal activity.

Vertical, aligned cracks are detectable by their seismic anisotropy signature. Shear-wave splitting and polarization measurements [7–9], for example, are often used to detect the presence of anisotropy. Another means of detecting seismic anisotropy is with a network of receivers and shots that records P-wave travel times as a function of the receiver to shot azimuth θ. For an anisotropic medium, the travel time delays exhibit a $\cos(2\theta)$ variation (e.g., [10]). The fast direction of energy propagation indicates the direction of the average crack alignment, whereas the magnitude of the anisotropy provides a measure of the crack density. Quantitative measurements of crack-induced anisotropy have been made in a variety of oceanic settings, including along mid-ocean ridge crests [11–14], in older (>1 Ma) oceanic crust [7–9,15,16], on ocean islands [17], and in back-arc basins [18]. In these studies the anisotropy is predominantly restricted to the shallowest crust, seismic layer 2, where the porosity is in general the highest [19].

2. Experiment and methods

To quantify the anisotropic properties of the crust formed at a fast-spreading ridge and to estimate the distribution and degree of aligned versus non-aligned pore space, we analyzed data from a seismic tomography experiment located near 9°30′N on the East Pacific Rise (Fig. 1). The seismic data were collected in 1988 as part of a three-dimensional tomography experiment that was designed to determine the velocity structure of the crustal magmatic system beneath a fast-spreading ridge [20–22]. Here, we analyze P-wave travel time data whose ray paths traverse the upper 4 km of the crust. This experiment provides excellent spatial and azimuthal ray coverage and allows us to determine the seismic anisotropic and isotropic properties of the shallow crust. De-

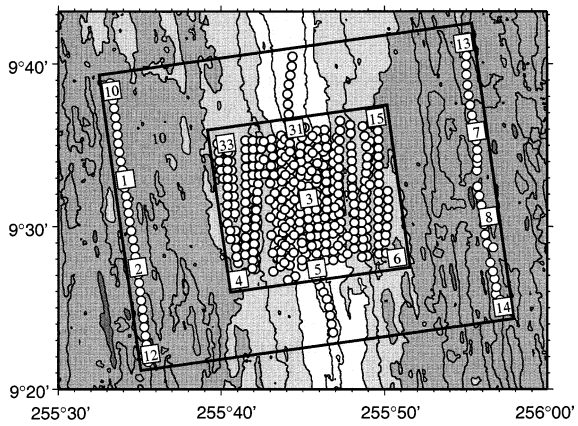

Fig. 1. Seafloor bathymetry and geometry of the seismic tomography experiment. The local rise trend and orientation of the experiment are N8°W. Bathymetry is contoured at 100 m intervals, gray shade changes every 200 m. An array of 15 ocean bottom receivers, seven near- and eight off-axis instruments (numbered squares), recorded data from about 480 explosive sources (small circles), for a total of 3080 primary crustal arrivals. The aperture of the experiment is 42×31 km^2. The local, full spreading rate is $\sim$11 cm yr^{-1}.

scriptions of the instruments, the shots, and their locations can be found in Fig. 1 and in [20–22].

Our analysis includes an examination of P-wave travel time residuals calculated from seismic models containing no anisotropy or a fixed percentage of anisotropy and direct inversion of the data for anisotropic and isotropic structure. The forward modeling of travel times and the inversion procedure follow that of Toomey et al. [21] and Dunn et al. [22] and are modified to include anisotropy with an hexagonal symmetry system, where the symmetry axis is confined to the horizontal plane [14]. This symmetry system is useful for vertical, aligned cracks in the shallow crust (e.g., [10]). The percent anisotropy is defined as: $100\%\times(V_{p,max}-V_{p,min})/V_{p,average}$, where V_p is the P-wave velocity. The starting velocity model is a one-dimensional (depth-dependent) isotropic model taken from [21] (Fig. 2a). The model consists of a $42\times31\times4$ km^3 volume with a horizontal grid spacing of 250 m and a vertical spacing of 200 m for ray tracing and a horizontal grid spacing of 750 m and a vertical spacing of 200 m for the isotropic perturbations. The anisotropic perturbational model is a function of depth only,

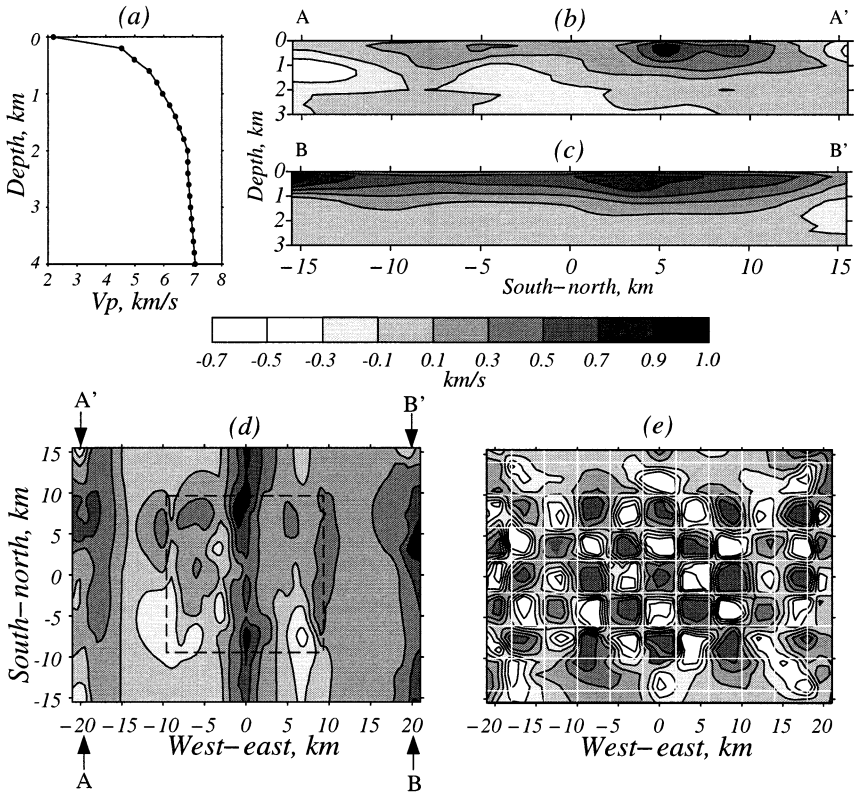

Fig. 2. (a) Average, one-dimensional velocity structure used as a starting point for the tomographic inversions. (b,c) Vertical slices through the shallow crustal tomography model located beneath the westernmost and easternmost refraction lines, respectively. Perturbations with respect to the starting model are contoured at intervals of 0.2 km s^{-1}. This model was constructed using four iterations of the forward and inverse problem with $\lambda_h = \lambda_v = 125$ (see [21] for details). (d) A horizontal slice through the model at 600 m depth. Dashed box indicates spatial extent of the previous tomographic imaging of Toomey et al. [21] and corresponds to the inner box of Fig. 1. Model resolution, which depends on the density and angular distribution of rays, is estimated with the reconstruction of a 'checkerboard' model. Travel times are computed from a model with 3 km blocks of ± 0.5 km s^{-1} using a fixed ray set (rays calculated with respect to the three-dimensional isotropic model of b–d) and Gaussian noise with a standard deviation of 13 ms is added. The synthetic data are then inverted using the same model parameterization used with the real data. A map view section at 600 m depth (e) shows that highs and lows are properly reconstructed over most of the model space, but their magnitudes may be under-represented. In addition, a smaller 2 km checkerboard pattern was well constructed beneath the outer refraction lines and within the dashed box of panel d.

with a 200 m spacing. The inverse problem is regularized by assigning smoothness constraints on the form of the model and by assigning uncertainties of 20% in isotropic velocity and, when also solving for anisotropy, 10% in percent anisotropy and 15° in azimuth of the fast axis of anisotropy. Vertical and horizontal model smoothnesses are controlled by independent weighting values (λ_v and λ_h, respectively), which allow the user to control the trade-off between the data misfit and model smoothness. The normalized misfit, $\chi^2 = (1/N)(\mathbf{d}-\mathbf{Gm})^T\mathbf{C}_d^{-1}(\mathbf{d}-\mathbf{Gm})$, provides a weighted measure of the data misfit with respect to a velocity model, where N is the number of data, $\mathbf{d}$ is the data vector, $\mathbf{G}$ is the Frechet matrix, $\mathbf{m}$ is the model vector, and $\mathbf{C}_d$ is a diagonal matrix composed of individual travel time uncertainties. If the data uncertainties are known accurately, a solution can be chosen objectively by selecting one whose degree of smoothness results in a χ^2 value near one [23].

3. Results

We first inverted the data for isotropic three-dimensional velocity structure. The preferred isotropic model (Fig. 2b–d) achieves a final χ^2 misfit of 1.2 after four iterations. Smoother models yielded similar results except that the χ^2 misfit is higher and model perturbations are of lower magnitudes. Rougher models do not appreciably reduce the χ^2 misfit. Our preferred model is similar to that obtained by Toomey et al. [21], who imaged shallow crustal structure within a smaller area (18×18 km^2) centered on the rise (inner box of Figs. 1 and 2d). Our model provides additional constraints on isotropic structure at distances greater than 10 km from the rise axis. At these distances, velocities are generally faster to the east than to the west and increase with crustal age. Beneath the outer two rise-parallel shot lines (20 km to either side of the rise), velocities are up to 0.9 km s^{-1} faster than average (i.e., the starting model) and vary along the rise by up to 0.6 km s^{-1}.

Fig. 3a shows the final travel time residuals for the preferred isotropic model plotted as a function of receiver-shot azimuth (θ). There is a good azimuthal ray coverage in the shallow crust and evidence for a systematic cos(2θ) dependence to the travel time residuals for ray paths that turn in the upper 2 km of the crust (upper plot, Fig. 3a). The cos(2θ) curve that best fits the data has a peak-to-peak amplitude of 12 ms and a phase shift that aligns the fastest azimuthal direction along a line rotated 6° counterclockwise from the rise trend (N8°W).

We tested for simple spatial variations in anisotropy by analyzing the residual patterns for selected groups of receivers and shots (Fig. 4). The best-fitting cos(2θ) curve for residuals whose ray paths lie entirely to the west of the rise is similar to that for residuals whose ray paths lie to the east of the rise (Fig. 4a,b). We also tested for a systematic dependence of anisotropy with crustal age and found that the amplitudes of the best-fitting cos(2θ) curves decreased with distance from the rise, such that stations located 20 km from the rise recorded no distinguishable cos(2θ) pattern (Fig. 4c–e). However, since azimuthal ray coverage decreases with the distance of a station from the experiment's center, any anisotropic sig-

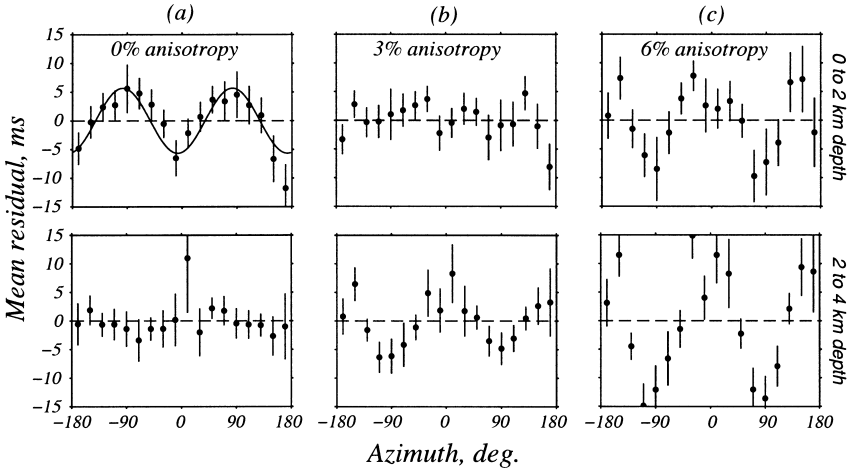

Fig. 3. Mean travel time residual versus source receiver azimuth for ray-turning depths of 0–2 km (upper figures), and 2–4 km (lower figures). The azimuth is measured at the receiver and clockwise from the trend of the rise (N8°W), in a horizontal plane. The data are binned and a mean is determined for each bin so that each point represents the mean residual of a 20° azimuth bin. The vertical bars represent the 95% confidence interval of an estimated mean, as determined by Student's t-test. (a–c) Residuals for imposed anisotropy of 0, 3, and 6%, respectively (see text). Also shown in panel a is the cos(2θ) curve that best fits those residuals. As the amount of anisotropy is increased to 6%, the cos(2θ) pattern decreases in amplitude and then changes sign. From 0 to 2 km depth, the average amount of anisotropy that best fits the data is about 3%. Below 2 km depth, an isotropic model best fits the data.

nal recorded by the outermost instruments may be mapped into isotropic velocity heterogeneity. Furthermore, for the outermost receivers, the ray turning depths are on average deeper than for other receivers and thus may not uniformly sample the shallowest crust that contains the anisotropy. Therefore, the apparent decrease in anisotropy may not be realistic. Lastly, we found anisotropy to be present in young, 0–40 000 yr old, crust. For shots within 5 km of receiver 3 (see Fig. 1), the ray paths turn within 0–2.5 km of the rise, and their residuals exhibit a pattern whose best-fitting cos(2θ) curve has a peak-to-peak amplitude of 20 ms (Fig. 4f).

We explored the magnitude of seismic anisotropy consistent with the data by carrying out tomographic inversions for models with a single fixed percentage and direction of anisotropy, while solving for three-dimensional isotropic structure. Test cases ranged from 1 to 6% anisotropy and in each case it was assumed that the fast axis of anisotropy was oriented N14°W (on the basis of the residual pattern of Fig. 3a). Except for the addition of anisotropy to the starting model, the inversion parameterization and method were the same as that used for the best isotropic model above. The final isotropic models for the cases with 0–4% anisotropy were all similar. Higher percentages of anisotropy resulted in models that were noticeably different, but the maximum difference did not exceed 0.3 km s^{-1}. Fig. 5 shows the final misfit for each model after four iterations of the forward and inverse problems. Of these models, which contain a constant magnitude of anisotropy everywhere, the data are best fit with a model containing 2% anisotropy.

Examination of the form of the residuals for cases with 0, 3, and 6% anisotropy as a function of azimuth and for different ray turning depths (Fig. 3) provides further insight into the amount of anisotropy that is allowed by the data. As the amount of assumed anisotropy increases, the amplitude of the cos(2θ) curve of the residuals decreases and then changes sign, such that the 6% model overcorrects the cos(2θ) variation at all depths. The model with 3% constant anisotropy best fits the data for rays that turn between 0 and 2 km depth (Fig. 3b, upper plot). An isotropic

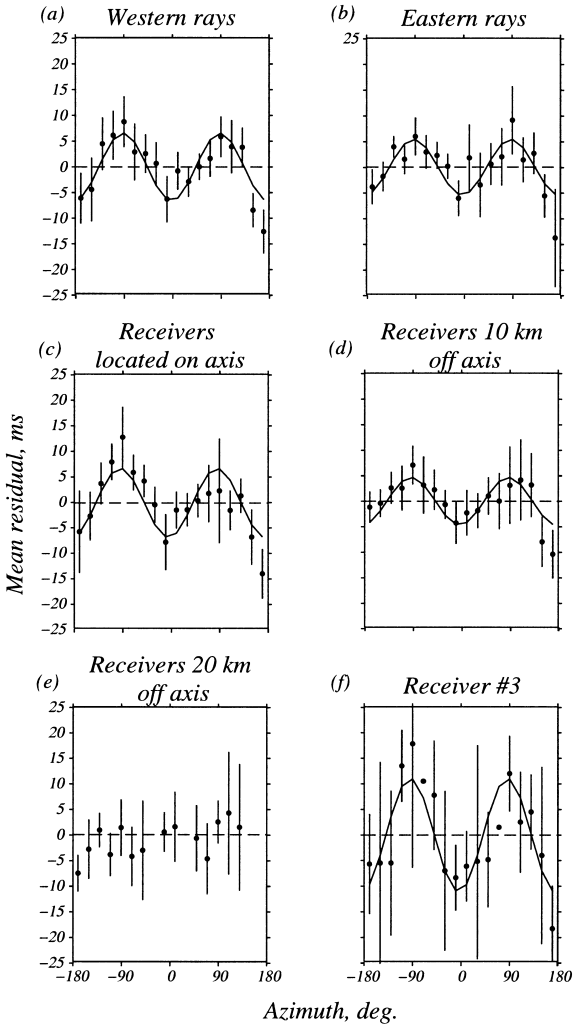

Fig. 4. Mean travel time residuals for different receiver-shot groupings. The azimuth is measured at the receiver and clockwise from the trend of the rise (N8°W), in a horizontal plane. The data have been binned as in Fig. 3. Also shown are the best-fitting cos(2θ) curves. (a) Shots and receivers located west of the rise; ray paths lie solely on the western side of the rise. (b) Shots and receivers located east of the rise; ray paths lie solely on the eastern side of the rise. (c) Receivers located on the rise axis; rays turn within 0–5 km of the rise axis. (d) Receivers located 10 km from the rise axis; rays turn within 5–10 km from the rise axis. (e) Receivers located 20 km from the rise axis; rays turn within 10–20 km of the rise. (f) Receiver 3, located in the center of the experiment and on the rise axis; ray paths turn within 0–2.5 km of the rise.

model best fits the data for rays that turn at 2–4 km depth (Fig. 3a, lower plot).

Finally, we performed inversions where both the percent anisotropy and angle of the fast axis of anisotropy were determined by the inversion itself (all other parameters were unchanged). The starting model was isotropic and the anisotropic solution was a function of depth only. The resulting model has approximately 4% anisotropy from 0 to 1 km depth, 2% from 1 to 2 km depth, and 0% below that (Fig. 6a). The upper 500 m of the model is not well constrained since most ray paths are oriented near vertically in this part of the model. The azimuth of the fast axis was determined to be ~N14°W (6° west-of-north of the rise trend). The azimuth, however, is not well constrained and may be in error by as much as 10°. Changes larger than about 10–15° give rise to significantly larger travel time misfits. Inspection of the final form of the residuals (Fig. 6b) shows that the inversion has removed the original cos(2θ) signal in Fig. 3a. Similar results were found when the starting model contained 2% anisotropy everywhere. This depth-dependent model achieves a significant improvement in data misfit ($\chi^2 = 1.01$) over the previous models with constant anisotropy or no anisotropy (Fig. 5). Additionally, the maximum difference between the final isotropic portion of this model and the purely isotropic model determined previously (Fig. 2) is not significant (< 0.2 km s^{-1}), indicating that the trade-off between anisotropic and isotropic parameters is not significant to the interpretation of the isotropic component of the model.

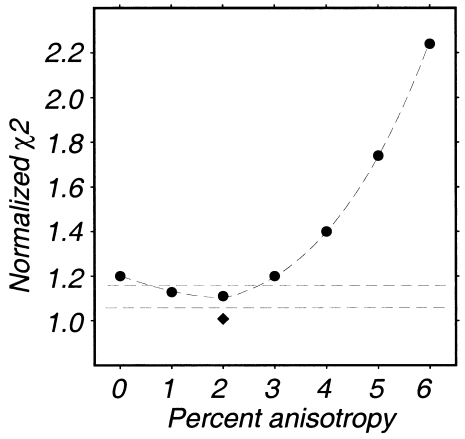

Fig. 5. The normalized travel time misfit χ^2 versus percent anisotropy. Different amounts of uniform anisotropy (0–6%) were included in the starting model with the fast axis of anisotropy aligned N14°W (6° west-of-north from the rise trend). The data were then inverted for the best-fitting isotropic structure. The dashed lines indicate the 2σ uncertainty of the model with 2% constant anisotropy. The diamond symbol indicates the χ^2 value for the model with depth-dependent anisotropy as determined by a tomographic inversion (Fig. 6a). This model provides a significantly better fit to the data than achieved by models with constant anisotropy.

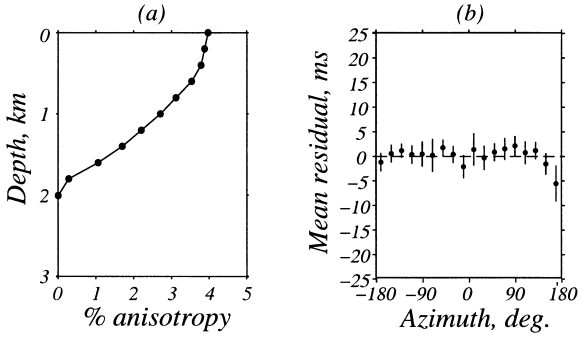

Fig. 6. (a) Percent anisotropy versus depth as determined by an inversion of the data. (b) Final mean travel time residuals versus receiver-to-source azimuth for rays turning at depth of 0–2 km (similar to Fig. 3a). The joint inversion for anisotropy and isotropic heterogeneity has removed the cos(2θ) pattern that was present in Fig. 3a.

4. Discussion

4.1. Isotropic structure

Large lateral variations in isotropic velocity were detected, whose origins likely lie in the distribution of pores, cracks, and alteration products. The seismic results for the axial region (inner box, Figs. 1 and 2d) have been discussed previously [21]. Beyond the axial region, the observed increase in velocity with distance from the rise is consistent with a general observation that shallow crustal velocities increase with crustal age (e.g., [24,25]). This trend is generally attributed to the filling of pore space with hydrothermal alteration products (e.g., [26–28]), although other factors may also be important [29,30]. Slower velocities

to the west of the rise than the east are likely the result of a thicker layer 2 to the west [31]. The data rule out the possibility of a significantly greater density of aligned cracks to the west (an increase in aligned cracks reduces the average velocity) because an east–west difference of 0.2 km s^{-1} in isotropic velocity requires a difference in anisotropy of $\sim$7% to lower the isotropic average, a value too large to be allowed by the data.

4.2. Anisotropy structure

The observed cos(2θ) relationship for crustal P-wave travel times is consistent with crack-induced anisotropy for vertical cracks aligned within a few degrees of the trend of the rise axis [8,10,32]. Although not well constrained, the alignment direction as estimated from the seismic results roughly agrees with seafloor observations of crack orientations that are oriented subparallel to the rise trend [1,33]. The 2θ pattern indicates that the travel time signal is dominated by cracks with aspect ratios >0.01 (thinner cracks give rise to a dominant cos(4θ) signal [34]). Using Hudson's crack theory [34] and 4% anisotropy, aligned cracks with aspect ratios of 0.01–0.1 give rise to porosities of $\leq$1%.

On average, seismic velocities, which vary inversely with porosity, are low in the shallow crust and increase with depth. The introduction of aligned cracks to an uncracked basalt, such that 4% seismic anisotropy is produced, is not sufficient to reduce the average velocity of the basalt in its uncracked state ($\sim$6–7 km s^{-1}) to the velocities observed in the shallow crust ($\sim$3–5 km s^{-1}; Fig. 2a). Cracks producing 4% anisotropy lower the average velocity of the rock by only 0.14 km s^{-1}. Therefore, the low velocities in the shallow crust (<2 km depth), with respect to the deeper crust, require the presence of one or more additional mechanisms for decreasing seismic velocity, such as the presence of non-aligned cracks, variations in pore pressure with depth [29], a higher vesicularity of the rock [29,31,35–37] that is perhaps, but not necessarily, related to a higher proportion of porous extrusive rocks to low-porosity sheeted dikes [20,29,38–40], or a difference in metamorphic grade [29,41]. At 500 m depth the average P-wave velocity is about 5 km s^{-1}. This corresponds to a total of about 12% porosity using the theoretical calculations of Berge et al. [42] or the downhole logging results of Carlson and Herrick [43]. Therefore, seismically detectable, aligned cracks (providing $<1\%$ porosity) supply less than one-tenth of the total porosity of the shallow crust. Below 2 km depth, where no 2θ pattern is evident, aligned cracks may not exist, be closed by higher pressures, be cemented shut, or are too few in number to be seismically detectable.

Within ridge hydrothermal systems, fluid convection may follow rise-parallel cracks and faults (e.g., [2,44]). Our results indicate that seismically detectable, aligned cracks, which may act as fluid pathways, do not penetrate deeper than $\sim$2 km below the seafloor. However, in a previous study we have shown that the thermal structure of the axial magmatic system (estimated from the P-wave velocity structure) requires hydrothermal circulation into the lower crust [22]. Furthermore, ophiolite studies indicate that hydrothermal alteration penetrates into the lower crust [45]. These other studies indicate that a relatively high permeability can be achieved with only a few cracks or faults that are not detectable with the methods presented here.

The small proportion of aligned cracks relative to all cracks and pores suggests that fluids within seismically detectable, aligned cracks do not contain the bulk of the volume of hydrothermal fluids in the shallow crust. However, since porosity is not a general indicator of permeability, the seismic results alone cannot constrain the degree and orientation of fluid convection in the crust. To better understand the role of aligned cracks in the permeability structure of ridge hydrothermal systems, future approaches may include the use of seismic results along with other geological information to develop numerical models of hydrothermal circulation (e.g., [46–48]).

A comparison of our results with similar quality studies along intermediate- [13] and slow-spreading [14] ridges indicates that the crack-induced anisotropy of the shallow crust is not a function of spreading rate. In each case, detectable P-wave seismic anisotropy is restricted to the

upper ~2 km of the crust and the percent anisotropy is similar. Collectively, these results indicate similar densities of aligned cracks are present in these three different spreading environments. The data from each of these three experiments have been jointly inverted for velocity and anisotropy structure and the estimated magnitudes of anisotropy are considerably lower than in some previous experiments [11,12] that did not account for lateral velocity variations when estimating the anisotropy magnitude. As the isotropic velocity structure of intermediate and fast-spreading mid-ocean ridges is known to be largely two-dimensional, it may add an apparent azimuthal anisotropy to the data. An analysis of the anisotropy structure that does not take into account lateral variations in velocity structure may thus overestimate the magnitude of the crack-induced anisotropy.***RV***

References

[1] S.M. Carbotte, K.C. Macdonald, Comparison of seafloor tectonic fabric at intermediate, fast, and superfast spreading ridges; influence of spreading rate, plate motions, and ridge segmentation on fault patterns, J. Geophys. Res. 99 (1994) 13609–13691.

[2] R.M. Haymon, D.J. Fornari, M.H. Edwards, S. Carbotte, D. Wright, K.C. Macdonald, Hydrothermal vent distribution along the East Pacific Rise crest (9°09–54′N) and its relationship to magmatic and tectonic processes on fast-spreading mid-ocean ridges, Earth Planet. Sci. Lett. 104 (1991) 513–534.

[3] D.J. Wright, R.M. Haymon, D.J. Fornari, Crustal fissuring and its relationship to magmatic and hydrothermal processes on the East Pacific Rise crest (9°12′ to 54′N), J. Geophys. Res. 100 (1995) 6097–6120.

[4] K. Becker et al., Drilling deep into young oceanic crust, hole 504B, Costa Rica Rift, Rev. Geophys. 27 (1989) 79–102.

[5] P.A. Pezard, M. Ayadi, A. Revil, G. Bronner, R. Wilkens, Detailed structure of an oceanic normal fault: A multiscalar approach at DSDP/ODP Site 504, Geophys. Res. Lett. 24 (1997) 337–340.

[6] R.J.M. De Wiest, Geohydrology, Wiley, New York, 1965, 366 pp.

[7] R.A. Stephen, Seismic anisotropy observed in upper oceanic crust, Geophys. Res. Lett. 8 (1981) 865–868.

[8] R.A. Stephen, Seismic anisotropy in the upper oceanic crust, J. Geophys. Res. 90 (1985) 11383–11396.

[9] R.S. White, R.B. Whitmarsh, An investigation of seismic anisotropy due to cracks in the upper oceanic crust at 45°N, Mid-Atlantic Ridge, Geophys. J. R. Astron. Soc. 79 (1984) 439–467.

[10] V. Babuska, M. Cara, Seismic Anisotropy in the Earth, Kluwer Academic Publishers, Boston, MA, 1991, 217 pp.

[11] D.W. Caress, M.S. Burnett, J.A. Orcutt, Tomographic image of the axial low-velocity zone at 12°50′N on the East Pacific Rise, J. Geophys. Res. 97 (1992) 9243–9263.

[12] M.A. Macdonald, S.C. Webb, J.A. Hildebrand, B.D. Cornuelle, Seismic structure of the Juan de Fuca Ridge at 45°N, J. Geophys. Res. 99 (1994) 4857–4873.

[13] R.A. Sohn, S.C. Webb, J.A. Hildebrand, B.D. Cornuelle, Three-dimensional tomographic velocity structure of upper crust, CoAxial segment, Juan de Fuca Ridge: Implications for on-axis evolution and hydrothermal circulation, J. Geophys. Res. 102 (1997) 17679–17695.

[14] A.H. Barclay, D.R. Toomey, S.C. Solomon, Seismic structure and crustal magmatism at the Mid-Atlantic Ridge, 35°N, J. Geophys. Res. 103 (1998) 17827–17844.

[15] P.M. Shearer, J.A. Orcutt, Compressional and shear wave anisotropy in the oceanic lithosphere – the Ngendei seismic refraction experiment, Geophys. J. R. Astron. Soc. 87 (1986) 967–1003.

[16] R.S. Detrick, D.R. Toomey, J.A. Collins, Three-dimensional upper crustal heterogeneity and anisotropy around Hole 504B from seismic tomography, J. Geophys. Res. 103 (1998) 30485–30504.

[17] W. Menke, B. Bransdottir, S. Jakobsdottir, R. Stefansson, Seismic anisotropy in the crust at the mid-Atlantic plate boundary in south-west Iceland, Geophys. J. Int. 119 (1994) 783–790.

[18] N. Hirata, H. Nambu, M. Shinohara, K. Suyehiro, Seismic evidence of anisotropy in the Yamato Basin crust, Proc. Ocean Drill. Prog. Sci. Results 127–128 (1992) 1107–1121.

[19] P. Spudich, J.A. Orcutt, A new look at the seismic velocity structure of the oceanic crust, Rev. Geophys. 18 (1980) 627–645.

[20] D.R. Toomey, G.M. Purdy, S.C. Solomon, W.S.D. Wilcock, The three-dimensional seismic velocity structure of the East Pacific Rise near latitude 9°30′N, Nature 347 (1990) 639–645.

[21] D.R. Toomey, S.C. Solomon, G.M. Purdy, Tomographic imaging of the shallow crustal structure of the East Pacific Rise at 9°30′N, J. Geophys. Res. 99 (1994) 24135–24157.

[22] R.A. Dunn, D.R. Toomey, S.C. Solomon, Three-dimensional seismic structure and physical properties of the crust and shallow mantle beneath the East Pacific Rise at 9°30′N, J. Geophys. Res. 105 (2000) 23537–23555.

[23] S.C. Constable, R.L. Parker, C.G. Constable, Occam's inversion: A practical algorithm for generating smooth models from electromagnetic sounding data, Geophysics 52 (1987) 289–300.

[24] R.E. Houtz, J. Ewing, Upper crustal structure as a function of plate age, J. Geophys. Res. 81 (1976) 2490–2498.

[25] I. Grevemeyer, W. Weigel, Increase of seismic velocities in upper oceanic crust: The 'superfast' spreading East Pacific Rise at 14°14′S, Geophys. Res. Lett. 24 (1997) 217–220.

[26] R.S. Jacobson, Impact of crustal evolution on changes of the seismic properties of the uppermost ocean crust, Rev. Geophys. 30 (1992) 23–42.
[27] R.L. Carlson, Seismic velocities in the uppermost oceanic crust: Age dependence and the fate of layer 2A, J. Geophys. Res. 103 (1998) 7069–7077.
[28] R.H. Wilkens, G.J. Fryer, J. Karsten, Evolution of porosity and seismic structure of upper oceanic crust: importance of aspect ratios, J. Geophys. Res. 96 (1991) 17981–17995.
[29] G.M. Purdy, Observations of the shallow seismic structure of young oceanic crust, J. Geophys. Res. 92 (1987) 9351–9362.
[30] G.J. Fryer, D.J. Miller, P.A. Berge, Seismic anisotropy and age-dependent structure of the upper oceanic crust, in: J.M. Sinton, (Ed.), Evolution of Mid Ocean Ridges, AGU Geophys. Monogr. 57 (1989) 1–8.
[31] A.J. Harding, J.A. Orcutt, M.E. Kappus, E.E. Vera, J.C. Mutter, P. Buhl, R.S. Detrick, T.M. Brocher, Structure of young oceanic crust at 13°N on the East Pacific Rise from expanding spread profiles, J. Geophys. Res. 94 (1989) 12163–12196.
[32] S. Crampin, A review of the effects of crack geometry on wave propagation through aligned cracks, Can. J. Explor. Geophys. 29 (1993) 3–17.
[33] K.C. Macdonald et al., The East Pacific Rise and its flanks 8–18°N: history of segmentation, propagation and spreading direction based on SeaMarc II and Sea Beam studies, Marine Geophys. Res. 14 (1992) 299–344.
[34] J.A. Hudson, Wave speeds and attenuation of elastic waves in material containing cracks, Geophys. J. R. Astron. Soc. 64 (1981) 133–150.
[35] J.S. McClain, J.A. Orcutt, M. Burnett, The East Pacific Rise in cross section: A seismic model, J. Geophys. Res. 90 (1985) 8627–8639.
[36] K.M. Rohr, B. Milkereit, C.J. Yorath, Asymmetric deep crustal structure across the Juan de Fuca ridge, Geology 16 (1988) 533–537.
[37] E.E. Vera, J.C. Mutter, P. Buhl, J.A. Orcutt, A.J. Harding, M.E. Kappus, R.S. Detrick, T.M. Brocher, The structure of 0- to 0.2-m.y.-old oceanic crust at 9°N on the East Pacific Rise from expanded spread profiles, J. Geophys. Res. 95 (1990) 15529–15556.
[38] T.J. Herron, Lava flow layer – East Pacific Rise, Geophys. Res. Lett. 9 (1982) 17–20.
[39] G.L. Christeson, G.M. Purdy, G.J. Fryer, Structure of young oceanic crust at the East Pacific Rise near 9°30′N, Geophys. Res. Lett. 19 (1992) 1045–1048.
[40] A.J. Harding, G.M. Kent, J.A. Orcutt, A multichannel seismic investigation of upper crustal structure at 9°N on the East Pacific Rise: Implications for crustal structure, J. Geophys. Res. 98 (1993) 13925–13944.
[41] R. Detrick, J. Collins, R. Stephen, S. Swift, In situ evidence for the nature of the seismic layer 2/3 boundary in oceanic crust, Nature 370 (1994) 288–290.
[42] P.A. Berge, G.J. Fryer, R.H. Wilkens, Velocity–porosity relationships in the upper oceanic crust: theoretical considerations, J. Geophys. Res. 97 (1992) 15239–15254.
[43] R.L. Carlson, C.N. Herrick, Densities and porosities in the oceanic crust and their variations with depth and age, J. Geophys. Res. 95 (1990) 9153–9170.
[44] J. Yang, R.N. Edwards, J.W. Molson, E.A. Sudicky, Fracture induced hydrothermal convection in the oceanic crust and the interpretation of heat flow data, Geophys. Res. Lett. 23 (1996) 929–932.
[45] P. Nehlig, T. Juteau, Flow porosities, permeabilities, and preliminary data on fluid inclusions and fossil thermal gradients in the crustal sequence of the Samail Ophiolite (Oman), Tectonophysics 151 (1988) 199–221.
[46] N.D. Rosenberg, F.J. Spera, R.M. Haymon, The relationship between flow and permeability field in seafloor hydrothermal systems, Earth Planet. Sci. Lett. 116 (1993) 135–153.
[47] K. Latychev, R.N. Edwards, R.A. Sohn, Three-dimensional numerical modeling of hydrothermal circulation at the Co-Axial segment of the Juan de Fuca Ridge (abstract), EOS Trans. AGU 80 (Fall Meeting Suppl.) (1998) F858.
[48] A.S.M. Cherkaoui, R.A. Dunn, W.S.D. Wilcock, D.R. Toomey, Numerical models of hydrothermal cooling of the lower crust on the East Pacific Rise: thermal constraints from seismic tomography (abstract), EOS Trans. AGU 80 (Fall Meeting Suppl.) (1999) F1048.